Available online at www.sciencedirect.com
SCIENCE DIRECT
Polymer 46 (2005) 7273–7292
polymer
www.elsevier.com/locate/polymer

Microstructure and mechanical properties of microcellular injection molded polyamide-6 nanocomposites

Mingjun Yuan, Lih-Sheng Turng*

Polymer Engineering Center, University of Wisconsin-Madison, Madison, WI 53706, USA

Received 23 February 2005; received in revised form 25 May 2005; accepted 6 June 2005
Available online 19 July 2005

Abstract

The microstructure and mechanical properties of microcellular injection molded polyamide-6 (PA6) nanocomposites were studied. Cell wall structure and smoothness were determined by the size of the crystalline structure, which, in turn, were based on the material system and molding conditions. The correlation between cell density and cell size of the materials studied followed an exponential relationship. Supercritical fluid (SCF) facilitated the intercalation and exfoliation of nanoclays in the microcellular injection molding process. The orientation of nanoclays near the surface of microcells and between microcells was examined and a preferential orientation around the microcells was observed. Nanoclays in the microcellular injection molding process promoted the γ-form and suppressed the α-form crystalline structure of PA6. Both nanoclays and SCF lowered the crystallinity of the parts. Microcells improved the normalized toughness of the nanocomposites. Both microcells and nanoclay had a significant influence on the mechanical properties of parts depending on the molding conditions.

Keywords: Microcellular; Injection molding; Nanocomposites

1. Introduction

In recent years, intensive studies have focused on polymer nanocomposites in which at least one dimension of the dispersed phase was in the nanometer range. With the addition of platy nanofillers, nanocomposites exhibit superior properties such as enhanced mechanical and thermal properties, improved barrier performance, and flame retardancy [1–3]. Nevertheless, the initial commercialization of nanocomposites has been slow. This is primarily due to high material costs and challenges in fully and uniformly dispersing the nanofillers within the polymer matrix. More specifically, nanocomposites made from PA6 and layered silicate montmorillonite (MMT) have received much attention because of their high level of matrix–filler interaction involving ionic bonds with the silicate layers of the smectite group. The improved properties of PA6/MMT nanocomposites have been attributed to the high specific area and aspect ratio of the silicate layers as well as to the good matrix–filler interactions.

PA6 is an important engineering resin widely used in many applications as well as engineering processes such as injection molding, extrusion, and fiber fabrication. The primary chemical structure of aliphatic PA6 consists of amide groups separated by methylene sequences, where the hydrogen bonding ability to seek the maximum number of H-bonds within and between polymer chains is very strong. Maximization of H-bonds in the crystalline state of PA6 requires the polyamide chains to adopt either the fully extended or twisted configuration resulting in the different crystal forms [4–6]. PA6 usually crystallizes into the stable monoclinic α-form when the chains are in the fully extended zigzag conformation and grouped into essentially planar H-bonded sheets. The second stable crystalline structure of PA6 is the γ-form when the H-bonds are disposed on pleated extended sheets. The γ-form structure has a shorter chain axis dimension compared to the α-form due to a tilting of the amide group with respect to the chain axis. Owing to the H-bonding, the amide group conformation, and the tight fold formation of fast crystallization, PA6 also exhibits

* Corresponding author. Tel.: +1 608 262 0586; fax: +1 608 265 2316.
E-mail address: turng@engr.wisc.edu (L.-S. Turng).

0032-3861/$ - see front matter © 2005 Elsevier Ltd. All rights reserved.
doi:10.1016/j.polymer.2005.06.054

Table 1
L9 fractional orthogonal experimental design for PA6/MMT microcellular nanocomposites (NC5 and NC7.5) and PA6 microcellular neat resin (NR)

Trial for materials NC5, NC7.5, and NR	Melt temperature (°C)		Supercritical content (wt%)		Shot size (mm)		Injection speed (%)	
	Level	Setting	Level	Setting	Level	Setting	Level	Setting
1	1	232	1	0.2	1	16.5	1	20
2	1	232	2	0.4	2	18.4	2	40
3	1	232	3	0.6	3	20.5	3	60
4	2	243	1	0.2	2	18.4	3	60
5	2	243	2	0.4	3	20.5	1	20
6	2	243	3	0.6	1	16.5	2	40
7	3	254	1	0.2	3	20.5	2	40
8	3	254	2	0.4	1	16.5	3	60
9	3	254	3	0.6	2	18.4	1	20

some other crystalline structures such as the disordered pseudo-hexagonal γ*-form and β-form. Because of the lack of uniformity in the literature and the similarity regarding their structures, these two structures are usually not considered as separate PA6 structures [6,7].

The thermally stable α-form and the γ-form can be easily detected by X-ray diffractometry (XRD) and differential scanning calorimetry (DSC) techniques. The melting points of the α-form and the γ-form are reportedly 221 and 215 °C, respectively [8,9]. The values of the heat of fusion, ΔH_f^0, for the α-form and the γ-form are 241 and 239 J/g, respectively [10].

Microcellular foaming technology has emerged to meet the demand of reducing material consumption while not or only slightly deteriorating part properties. Microcellular foam is usually characterized by a cell size in the range of 1–100 μm. Depending on the materials used, microcellular foam can provide improved part properties ranging from increased thermal and acoustic insulation properties, higher strength/weight ratios, enhanced toughness and fatigue life, and even increased impact strength of parts [11–14] while using environmentally benign physical blowing agents. The advantages of microcellular structures have also attracted significant attention from the polymer society, which has led to the development of various microcellular foaming techniques applied to such processes as batch foaming [15–18], thermoforming [19], extrusion [20–22], and injection molding [23–26]. Among them, the microcellular injection molding process is one of the most promising methods and was first commercialized by Trexel, Inc. [26]. For the microcellular injection molding process, 'supercritical' nitrogen (N_2) or carbon dioxide (CO_2) is injected into the machine barrel and dissolved into a polymer melt to create a single phase polymer–gas solution that is capable of producing parts with a microcellular structure while using lower injection pressures, shorter cycle times, and less material. It also eliminates the need of a packing stage and improves the dimensional stability of the molded parts.

Substantial research and development have been conducted on the processing and characterization of many different microcellular- and filled-plastics [27–30]. However, the foaming process and cell structure of PA6 in microcellular processing are very difficult to control because of the high crystallinity and different thermomechanical histories of the materials. Recent studies have shown that the addition of nanoclay fillers greatly increases the viscosity of the polymer [31]. On the other hand, blending SCF into the polymer melt effectively reduces the viscosity and the glass transition temperature of the polymer melt, as well as the interfacial tension [32]. Hence, adding SCF into the nanocomposites renders a method to tailor the rheological and surface properties of the polymer to facilitate better microcell formation and improved mechanical properties, therefore, offering an opportunity to take advantage of the synergistic effect of combining the microcellular process with nanocomposite materials. This paper aims to examine the microstructures of microcells, nanoclay, and crystals in PA6 microcellular nanocomposites and the corresponding influence of nanoclay, crystallites, and microcells on part properties.

2. Experimental

2.1. Materials

Two commercial grades of PA6/MMT nanocomposites and their corresponding PA6 neat resin, namely, RTP-299-A-X-98284-A, RTP-299-A-X-98284-D, and RTP-299-A-X-98284-C provided by the RTP Company (USA), were studied. For the materials RTP-299-A-X-98284-A and RTP-299-A-X-98284-D, 5 and 7.5% MMT organoclays by weight were compounded into the PA6 neat resin matrix, respectively. In this study, these three materials are symbolized as NC5, NC7.5, and NR, respectively.

2.2. Melt processing

The materials were dried for 4 h at 100 °C under vacuum to remove moisture before use. The injection molding

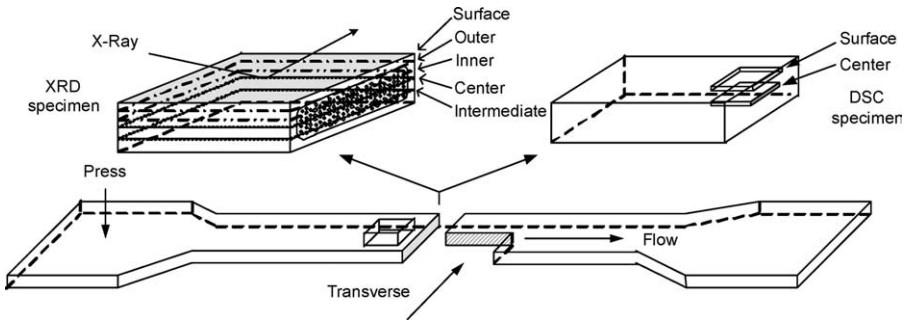

Fig. 1. Schematic of DSC and XRD specimen preparation.

experiments, based on an L9 design of experiments (DOE) scheme as specified in Table 1, were conducted on an industrial 150-ton TOYO injection molding machine equipped with SCF injection capability. The molding experiments were set to make standard ASTM-D638-02 tensile bars. SCF N_2 was used as the physical blowing agent to form the microcells in the parts. One additional molding trial, labeled as trial 0, was made for solid nanocomposite parts at the medium level of experimental settings with no SCF N_2 injection. These L9 experiments contain four different molding parameters (i.e. melt temperature, SCF weight percentage, shot size, and injection speed) at three different levels. For each trial in the L9 experiment, 60 samples were collected in the course of molding after discarding the first 20 samples.

All the materials (NC5, NC7.5, and NR) also underwent the compression molding process using a lab compression molder. During compression molding, flat sheets with a thickness of 1.5 mm were made at different cooling rates controlled by adjusting the press time and cooling water flow rates. For the fast cooling experiment, the material was melted at 255 °C for 6 min on the molding plate and then pressed with the mold resulting in cooling from 255 to 50 °C in 7 min. The slow cooling experiment was conducted by cooling the material from 255 to 50 °C over 1 h. There were also two intermediate cooling rates used by cooling the material from 255 to 50 °C for 20 and 40 min, respectively. The press force and press speed were kept constant for all experiments.

2.3. Testing techniques

2.3.1. Mechanical testing

The molded samples underwent the following mechanical tests: Tensile test and notched Izod impact test, following the ASTM-D-638-02 and the ASTM-D-256-02 standards, respectively. The tensile testing was done for all samples with a 0.5 N initial load, a constant crosshead speed of 5 mm/min, and a temperature of 25 °C on a MTS-Sintech-10/GL mechanical testing instrument. The Izod impact notching was done on a NOTCHVIS/CEAST notcher. Prior to impact testing, the notched specimens were conditioned at a temperature of 23 ± 2 °C and a relative humidity of $50\pm5\%$ for 48 h. Eight samples were tested for each molding trial for all materials used.

2.3.2. Scanning electron microscopy (SEM), transmission electron microscopy (TEM), and polarized optical microscopy (POM)

The microcellular structure of the molded parts was examined using a JOEL 6100 scanning electron microscope (SEM). The SEM specimens were taken from the middle of the molded dog-bone bar. The SEM specimens were characterized both along the melt flow direction and the transverse direction as shown in Fig. 1.

The TEM scanning of the specimens from as-received raw materials was executed on a JOEL JEM100CX TEM microscope to display the nanoclay dispersity in the raw materials before molding. The TEM scanning of the specimens from injection molded parts was performed on a LEO 912 EFTEM microscope to show the morphology of nanoclay in microcellular parts as well as in molded solid parts. To obtain better picture resolution, the objective aperture and energy filter were used in the LEO 912 EFTEM microscope. For the injection molded parts, the TEM specimens were made by cross-sectioning the block specimens from the microcellular injection molding experiments with an ultra-tome.

A Leitz Wetzlab polarized optical microscope was used to acquire the image of actual crystalline structures of PA6 in solid and microcellular injection molded parts. The injection molding samples were microtomed to prepare the POM film specimens with a thickness of 10 μm. The samples were cross-sectioned at the center of the molded solid and microcellular dog-bone bars.

For comparison, some POM specimens were also prepared by compressing and cooling the molten raw materials into solid films 10 μm thick on a hot-stage for materials NC5, NC7.5, and NR, respectively. The hot-stage specimens involved two different schemes: Slow cooling and fast cooling. Slow cooling was carried out by turning off the power of the hot-stage and letting the specimens fully cool down with the hot-stage. It usually took about 40 min. Fast cooling was performed by removing the specimens

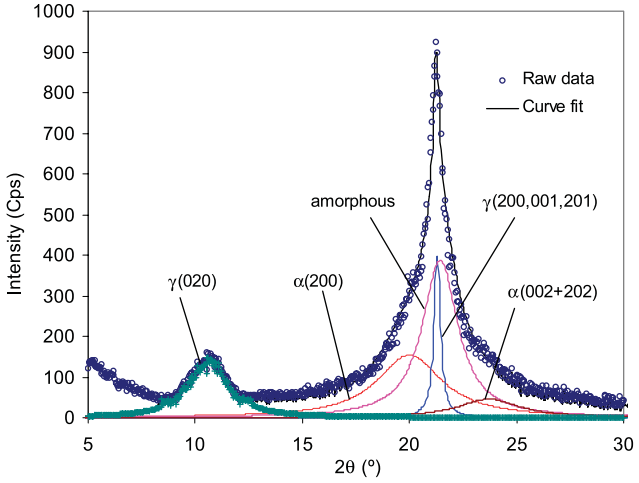

Fig. 2. XRD decomposition of the amorphous and crystalline forms.

from the hot-stage and letting them cool down naturally in the air for 15 min.

2.3.3. X-ray diffractometry (XRD)

XRD experiments were conducted using a STOE high resolution X-ray diffractometer with Cu Kα radiation at 40 kV and 25 mA. The XRD specimens were prepared in two different ways: For raw material pellets by compression molding, and for injection molded specimens by cutting and fine-polishing the dog-bone bars along different planes as shown in Fig. 1. The polishing procedure for injection molded specimens was done on a rotational station with 600 mesh and then 1200 mesh silicon carbide papers. The injection molded specimens were scanned in two different directions: Parallel and perpendicular to the melt flow direction. For the microcellular injection molded parts, there were visible solid surface layers. In order to analyze the crystalline structure and its orientation, XRD scanning surfaces from four different layers were prepared for the microcellular injection molded parts: On the dog-bone flat surface, on the central plane, on the plane called the 'outer' plane which separates the solid surface layer and the microcellular structural layer, and on the mid-plane designated as the 'inner' plane which is between the central plane and the outer plane. For the solid molded parts, since there was no obvious boundary layer, only three planes were chosen: The surface, the center, and the intermediate which is in the middle, between the surface and the central planes. The schematic of XRD specimen preparation is also shown in Fig. 1.

In order to quantitatively and qualitatively evaluate the contents of different crystalline forms present in both solid and microcellular parts of PA6 neat resin and PA6 nanocomposites, a Gaussian method mentioned in the literature [33–35] has been used to deconvolute the XRD peaks to obtain the relative crystallinity index (CI). Each resulting plot of X-ray intensity versus 2θ was modeled

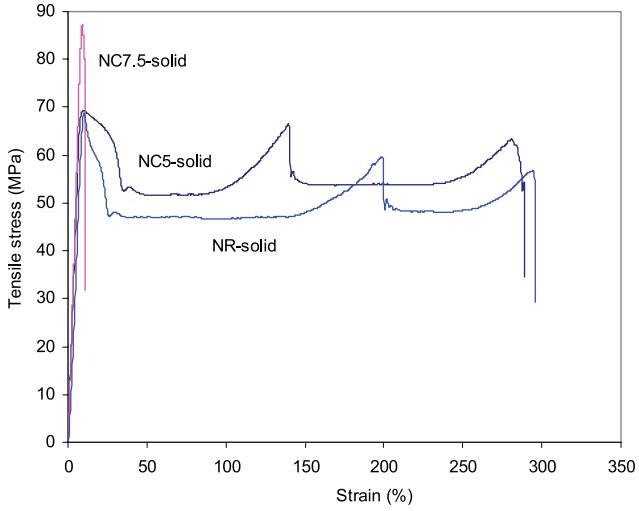

(a)

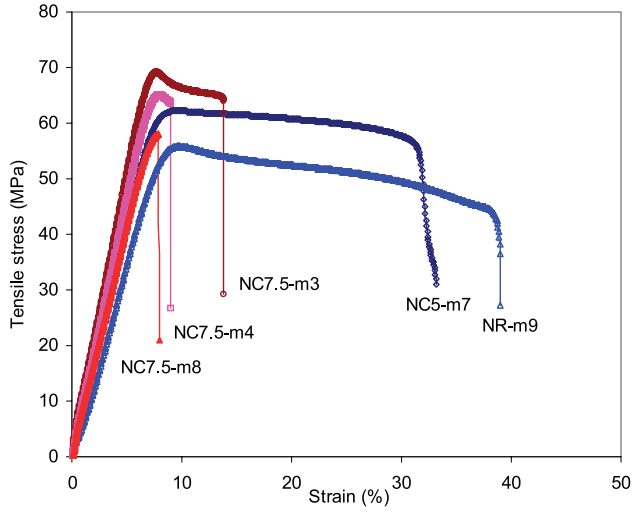

(b)

Fig. 3. Tensile stress versus strain curves of solid and microcellular parts: (a) Solid NR, NC5, and NC7.5 parts, (b) microcellular NR, NC5, and NC7.5 parts. The letter m denotes 'molding trial' and the number following denotes the 'trial number'.

using a Gaussian–Lorentzian peak shape in the profile fitting program PeakFit™ (AISN Software, Inc.). Areas of the peaks obtained from the analysis were used to estimate the degree of crystallinity for each form. In general, agreement between model predictions and the raw data yielded coefficients of determination, i.e. R^2, above 0.95. Depending on the materials used and the XRD scanning surfaces selected, two different schemes were used to calculate the confidence interval (CI) values, as depicted in Fig. 2 and in the following equations. With the appearance of the γ(020) peak, the area under the γ(020) peak is included in the calculations. Otherwise, the area under the γ(020) peak is taken to be zero.

$$\mathrm{CI}_{\alpha} = \frac{A_{\alpha(200)} + A_{\alpha(002)+\alpha(202)}}{A_{\alpha(200)} + A_{\alpha(002)+\alpha(202)} + A_{\gamma(020)} + A_{\gamma(001)+\gamma(200)+\gamma(201)} + A_{\mathrm{amorphous}}} \times 100\%$$

$$\mathrm{CI}_{\gamma} = \frac{A_{\gamma(020)} + A_{\gamma(001)+\gamma(200)+\gamma(201)}}{A_{\alpha(200)} + A_{\alpha(002)+\alpha(202)} + A_{\gamma(020)} + A_{\gamma(001)+\gamma(200)+\gamma(201)} + A_{\mathrm{amorphous}}} \times 100\%$$

$$\mathrm{CI}_{\mathrm{total}} = \mathrm{CI}_{\alpha} + \mathrm{CI}_{\gamma} = \frac{A_{\alpha(200)} + A_{\alpha(002)+\alpha(202)} + A_{\gamma(020)} + A_{\gamma(001)+\gamma(200)+\gamma(201)}}{A_{\alpha(200)} + A_{\alpha(002)+\alpha(202)} + A_{\gamma(020)} + A_{\gamma(001)+\gamma(200)+\gamma(201)} + A_{\mathrm{amorphous}}} \times 100\%$$

where $A_{\alpha(200)}$, $A_{\alpha(002)+\alpha(202)}$, $A_{\gamma(020)}$, $A_{\gamma(001)+\gamma(200)+\gamma(201)}$, and $A_{\mathrm{amorphous}}$ are the areas under each corresponding peak, respectively.

2.3.4. Dynamic mechanical analysis (DMA)

The dynamic mechanical properties of PA6 solid and microcellular injection molded parts were analyzed using a dynamic mechanical analysis instrument (DMA, Rheometrics DMTA-V). DMA specimens were taken from the middle section of the molded dog-bone bar. DMA specimens cut from molding samples were rectangular strips with dimensions of 40 mm by 4.5 mm by 3.3 mm. The DMA specimen thickness was kept the same as that of the molded sample. The specimen was annealed at 85 °C for 6 h before DMA testing. Measurements covered temperatures from a room temperature of 25 °C up to 220 °C at a heating rate of 2 °C/min, a frequency of 1 Hz, and 0.1% strain.

3. Results and discussion

3.1. Mechanical properties

3.1.1. Tensile and impact testing property

The tensile test results obtained from the solid PA6 neat resin and the solid PA6 nanocomposites are shown in Fig. 3(a). These results indicated that the mechanical behaviors of PA6 neat resin and PA6 nanocomposites differed significantly. For the PA6 neat resin, the highest value of stain at break was achieved at about 295%. The stress versus stain curves of the solid PA6 samples systematically showed two post-yielding peaks at a strain of approximately 195% and a strain at break, respectively. For the PA6 nanocomposite with 5 wt% clay, the higher tensile modulus and yield stress values were obtained with similar post-yielding phenomena. The two post-yielding peaks occurred at stains of approximately 130 and 280%, respectively. The appearance of the two post-yielding peaks closely relates to the strain hardening behavior of PA6 in both neat resin and nanocomposite forms.

The first peak after yielding is associated with a process called drawing. After yielding, the material in the neck stretches only to the natural draw ratio, which is a function of temperature and specimen processing, beyond which the material in the neck stops stretching and new material at the neck shoulders necks down. The neck then propagates until it spans the full gage length of the specimen. This necking process produces a dramatic transformation in the strengthened microstructure where the flat lamellar crystalline structures deform in the straining direction. As the strain increases further, the lamellar fragments rearrange with a dominantly axial molecular orientation to become what is known as the fibrillar microstructure. This structure requires a much higher strain hardening rate for increased strain.

The second post-yielding stress peak could be indicative of strain hardening due to slip of the aligned crystals as a result of cold drawing as well as crystallization of the amorphous regions distributed in the lamellar crystalline structure. With the strong covalent bonds now dominantly lined up in the load-bearing direction, the material exhibits markedly greater strengths and stiffnesses. Other factors such as the physical entanglements and the thermal mobility changes of the chains may also influence the strain hardening behavior during the test [36].

The span of strain values of PA6 nanocomposite NC5 between the yielding and the first post-yielding peak was obviously smaller than that of PA6 neat resin. This suggests that nanocomposite NC5 had a lesser drawing effect than PA6 neat resin. In comparison, PA6 nanocomposite with 7.5 wt% clay showed more brittle behavior. It had much higher tensile modulus and yield stress values than PA6 nanocomposite with 5 wt% clay and PA6 neat resin. PA6 nanocomposite with 7.5 wt% clay loading only showed slight necking with the value of strain at break around 11%.

Fig. 3(b) exemplifies the deformation behaviors of PA6 microcellular molded parts and PA6 microcellular nanocomposites at different molding conditions. In the graph, the letter *m* and the number following the material label denote 'microcellular' and the 'molding trial number,' respectively, according to Table 1. This notation will be used throughout this paper.

For the microcellular injection molded parts, no post-yielding peaks appeared in the testing. The representative data are plotted in Fig. 3(b). In most cases, a stable neck was formed shortly after yielding. With ongoing strain, the neck grew until ductile fracture occurred. PA6 nanocomposites had higher tensile modulus and yield stress values than PA6 neat resin. With higher clay loading, the higher tensile modulus and yield stress values were to be expected. Both

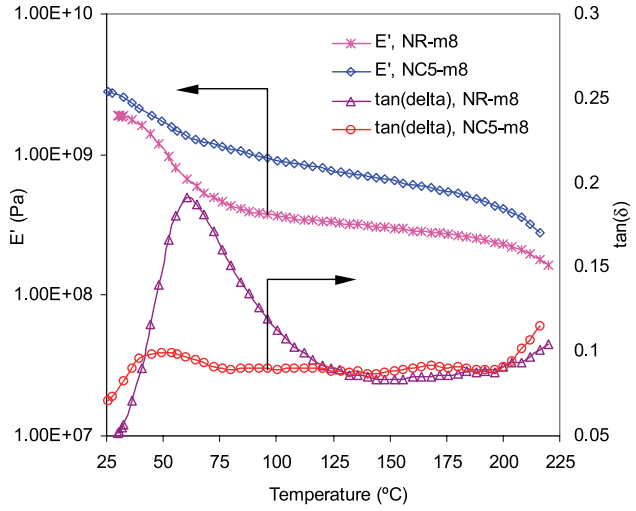

Fig. 4. Storage modulus E' and tan(δ) for PA6 microcellular neat resin and PA6 microcellular nanocomposite parts.

PA6 neat resin and PA6 nanocomposite with 5 wt% clay had much smaller values of strain at break than their corresponding solid counterparts. However, with the 7.5 wt% clay loading, the value of strain at break at around 13% of the microcellular part from molding trial 3 was slightly higher than that of its corresponding solid part.

From Fig. 3(b) it can also be seen that the tensile testing behaviors of microcellular parts are strongly dependent on the molding conditions. With microcellular molding trial 8, almost no clear necking behavior was observed for PA6 nanocomposite with 7.5 wt% clay. The crazing of the NC7.5-m8 microcellular nanocomposite part occurred at the end of the linear region (elastic region) of the stress–strain curve of the tensile bar. It is clear that optimal molding conditions exist for the microcellular molding process where better tensile properties, such as higher tensile modulus and yield stress as well as larger strain at break, can be achieved.

In studying the fracture mechanism of PA6/MMT nanocomposite tensile specimens, Uribe-Arocha et al. reported a phenomenon where multiple voiding in the core caused initial failure and a sheet-like structure to be formed in the fracture surface of the tensile specimens [37]. With this proposed mechanism, it is possible to assume that these initial voids form when the material fibrils break down and the microscopic fractures open up as the tensile loading increases. However, the dimension of the voids for initiating and propagating the fracture is not mentioned in the study. For the microcellular injection molded PA6 neat resin and PA6 nanocomposite parts, some microcells are already in existence in the parts. Their effect on the tensile fracture mechanism is still unknown. It was observed that although PA6 neat resin is generally considered a ductile material, the PA6 microcellular neat resin and PA6 microcellular nanocomposite parts suffered notch-brittleness to some extent. This indicates that the cells formed in the microcellular molding process likely behaved as voids. More detailed results of the study can be found in Ref. [38].

3.1.2. Dynamic mechanical property

The dynamic storage modulus as well as the tan(δ) versus temperature traces for the microcellular neat resin and the microcellular nanocomposite parts are shown in Fig. 4. With the addition of nanoclay, the storage or elastic modulus (E') of PA6 microcellular nanocomposite is higher than that of PA6 microcellular neat resin. The storage modulus curve of PA6 microcellular nanocomposite with respect to temperature is also flatter than that of PA6 microcellular neat resin. These phenomena follow the trend of the solid PA6 neat resin and PA6 nanocomposites. The phase angle curves of both the microcellular neat resin and the microcellular nanocomposite parts have dynamic relaxation peaks at around 60.3 and 49.0 °C, respectively. These peaks are referred to as α relaxation peaks of PA6 in these microcellular parts. These α relaxation peaks are believed to be related to the breakage of hydrogen bonding between PA6 chains, which induces long range segmental chain movement in the amorphous area [39,40]. Correspondingly, the temperatures at the peaks are assigned to the glass transition temperature of PA6 in the microcellular parts. The flat storage modulus and phase angle curves of microcellular nanocomposites also suggest a strong interaction between the PA6 matrix and the nanoclay platelets.

3.1.3. Normalized mechanical properties

The DOE (design of experiments) study showed that the structure and mechanical properties of the microcellular parts depended on the materials (e.g. the nanoclay content) and on the molding conditions. Among all of the molding parameters, the shot size, which is the amount of material injected into the mold cavity, was the most predominant molding parameter, affecting the cell size, cell density, and tensile strength of the microcellular neat resin and microcellular nanocomposites. The order of importance of the other parameters varied with the materials used and the nanoclay content. The order also changed with respect to the cell size, cell density, and tensile strength.

With the addition of nanoclay, a higher weight reduction value for the microcellular part was achieved. Based on the experimental results of this study, the maximum weight reduction rate for microcellular nanocomposites was up to 25–30% while only 20–25% was achieved for the microcellular neat resin. At this weight reduction rate, the part geometry can still be kept without the incomplete filling problem. The higher weight reduction rate for microcellular nanocomposites can be attributed to the higher content of SCF being able to dissolve into and be trapped in the PA6 matrix when the nanoclay is added.

In studying the roles of crystallinity and reinforcement in the mechanical behavior of the PA6/MMT nanocomposite, Bureau et al. concluded that improvements in rigidity and strength observed when MMT was added to PA6 were

Table 2
Variations of normalized tensile strength per unit mass of microcellular injection molded parts (in percent)

Molding trial no.	Neat resin NR with microcells Clay content 0.0 wt%	Nanocomposite NC5 with microcells Clay content 5.0 wt%	Nanocomposite NC7.5 with microcells Clay content 7.5 wt%
0	0.0	24.9	29.9
1	−1.1	−5.8	0.6
2	−6.6	2.4	0.8
3	−4.5	8.8	9.7
4	−8.7	0.4	6.2
5	−8.9	9.2	13.2
6	−8.0	−7.0	2.3
7	−13.0	7.5	6.6
8	−7.3	−7.0	−0.2
9	−10.1	3.9	2.1

related to the reinforcing filler and not to a modification of the crystalline structure [7]. With regard to microcellular nanocomposites, the molding process was more complicated. In the microcellular injection molding process, nanoclay changed not only the PA6 crystalline structures but also the microcellular structures. Thus three different structural components directly affected the mechanical properties of the part including the crystalline structures, microcells, and nanofillers.

In order to differentiate the respective effects associated with the reinforcing nanoclay and those associated with the microcells on the mechanical properties, the rule-of-mixture is assumed to be valid for simplicity. The values for the tensile strength and tensile modulus, normalized with respect to the solid PA6 neat resin, are shown in Tables 2 and 3. The experimentally measured values and the properties of solid PA6 neat resin and solid PA6 nanocomposite (from molding trial no. 0) as the base values were used in the rule-of-mixture calculation. In this method, it is assumed that the final mechanical properties of the PA6 microcellular nanocomposite were the sum of that of the solid PA6 neat resin and the property changes caused by the presence of cells and nanoclay particles, respectively. The normalized toughnesses of the microcellular parts with respect to their corresponding solid parts are shown in Fig. 5. The toughness is defined as the total area under the stress–strain curve up to fracture. This area is the total mechanical energy per unit volume consumed by the material in straining it to fracture. It has the same units as the tensile stress or modulus and is often termed the 'modulus of toughness'.

Previous studies have shown that the γ-form has lower inherent strength but higher ductility [7,41]. The results from the XRD and DSC analysis of this study revealed that the addition of nanoclay resulted in a slightly lower crystallinity with the γ-form taking precedence. Thus it is the reinforcing nanoclay rather than a modification of the crystalline structure that is responsible for the improved tensile strength and modulus. Tables 2 and 3 show that for the microcellular parts, the detrimental effect of microcells on the tensile strength and modulus has a comparable magnitude to that of the improvement gained by the addition of nanoclay. Depending on the molding conditions, the results from the combined effect of microcells and nanoclay could be either improved performance or decreased material properties. On the other hand, the microcells improved the normalized toughness of nanocomposites.

With higher nanoclay loading, more improvement could be achieved as shown in Fig. 5(a). This improvement results from two different aspects: The crystalline structure modification due to the nanoclay addition, and the microcells acting as the crack arrestors, as shown in

Table 3
Variations of normalized modulus per unit mass of injection molded microcellular parts (in percent)

Molding trial no.	Neat resin NR with microcells	Nanocomposite NC5 with microcells		Nanocomposite NC7.5 with microcells	
	Clay content 0.0 wt%	Clay content 5.0 wt%		Clay content 7.5 wt%	
		Cell effect	Cell and filler effect	Cell effect	Cell and filler effect
0	0.0	0.0	6.0	0.0	37.1
1	−4.4	−1.8	4.2	−2.2	34.9
2	−5.2	−6.2	−0.2	−5.9	31.2
3	−12.1	0.6	6.6	−7.7	29.4
4	−6.7	6.6	12.6	−13.1	24.0
5	−2.8	6.5	12.5	−17.8	19.3
6	−5.7	1.6	7.6	−28.8	8.3
7	−5.6	−3.0	3.0	−19.5	17.6
8	−7.8	−1.6	4.4	−30.5	6.6
9	−7.9	12.4	18.4	−25.9	11.2

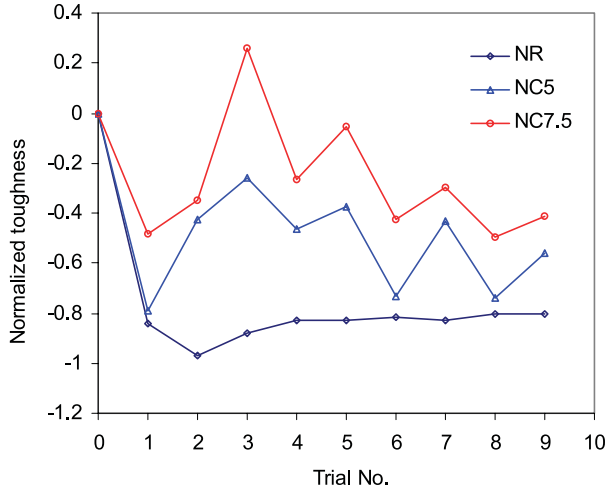

(a)

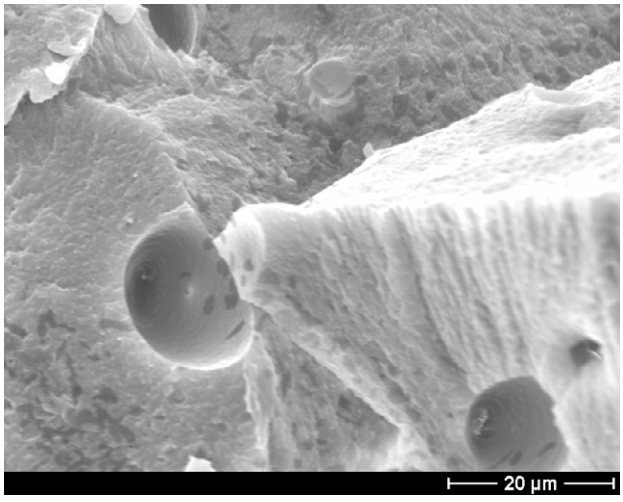

(b)

Fig. 5. Normalized toughness and crack arrestor of microcellular parts: (a) Normalized toughness versus molding trial, (b) cell acting as a crack arrestor for microcellular nanocomposite NC7.5.

Fig. 5(b). After normalizing the toughness of microcellular neat resin and nanocomposite parts with respect to the solid neat resin part, and by comparing the normalized tensile strength and modulus in Tables 2 and 3 with the normalized toughness, it was found that with a proper amount of nanoclay and the proper molding conditions, it is possible to obtain a better normalized tensile strength while achieving an improved normalized toughness. The favored molding conditions correspond to the higher level shot size and the medium or high level SCF content.

3.2. Microstructures

3.2.1. SEM morphology

Typical SEM micrographs of microcellular structures of PA6 neat resin and PA6 nanocomposites are shown in Fig. 6. These structures were obtained from the dog-bone

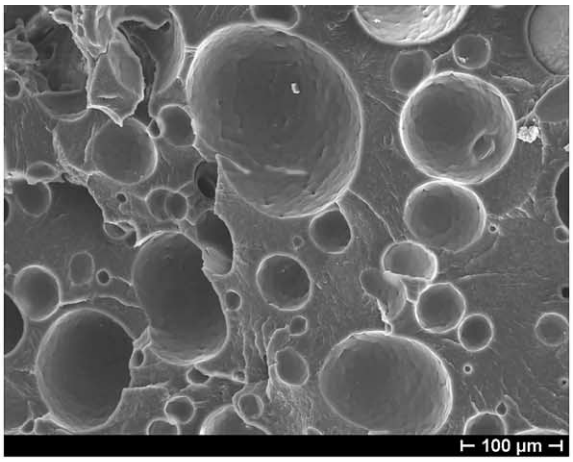

(a)

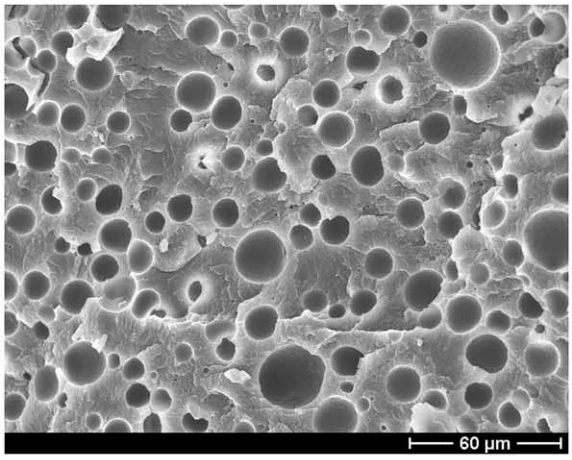

(b)

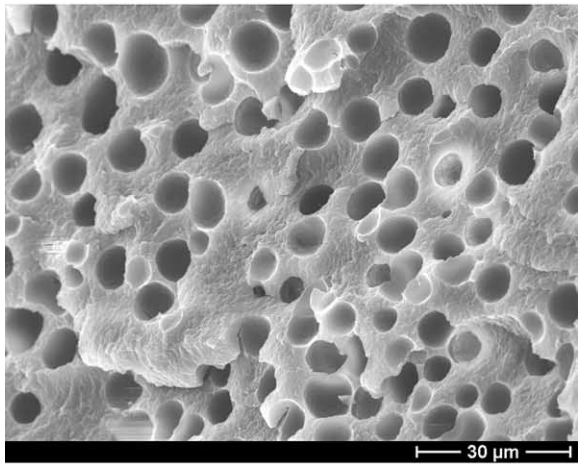

(c)

Fig. 6. Microstructures of cells in the cores of various samples with the microcellular molding conditions of trial 9: (a) Neat resin NR, (b) PA6 nanocomposite NC5, (c) PA6 nanocomposite NC7.5.

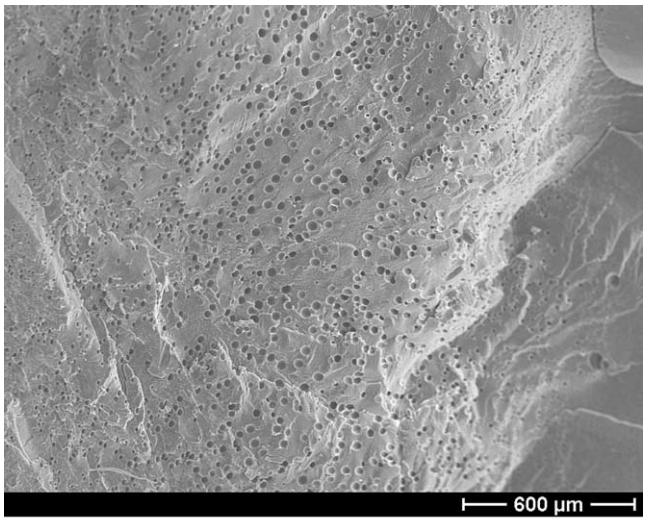

(a)

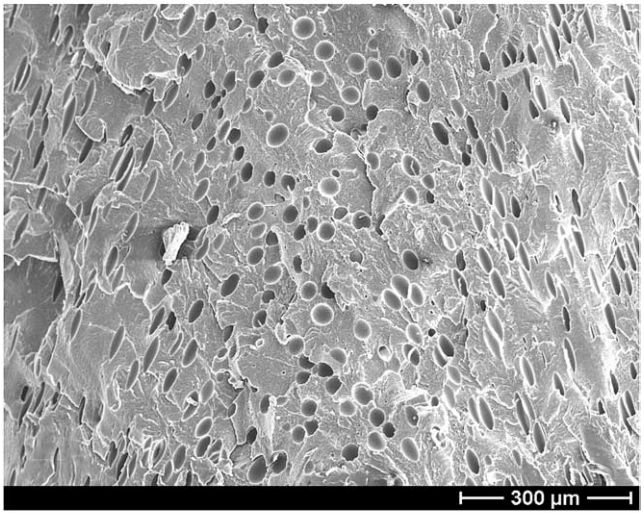

(b)

Fig. 7. Microstructures of cells viewed from different cross-sections for microcellular nanocomposite NC5 molded at trial 5: (a) Normal to the flow direction, (b) parallel to the flow direction.

parts produced under the same microcellular molding conditions of trial 9 but with different materials. For this molding trial, PA6 neat resin exhibited non-uniform cell structures with an average cell size of about 41 μm and a cell density of about 2.5×10^6 cells/cm^3. PA6 nanocomposite NC5 with 5 wt% nanoclay generated smaller and denser cells with an average cell size of about 10 μm and a cell density of about 2.3×10^8 cells/cm^3. PA6 nanocomposite NC7.5 with 7.5 wt% nanoclay gave rise to an even finer structure with a cell size of about 8.6 μm and a cell density of about 5.3×10^8 cells/cm^3.

With the addition of nanoclay, the cell density increased over two orders of magnitude and the cell size was reduced to one-fourth of that of the PA6 neat resin. The standard deviations of cell size for these materials were 18.8, 3.1, and 1.5 μm, respectively. Since the major difference in the

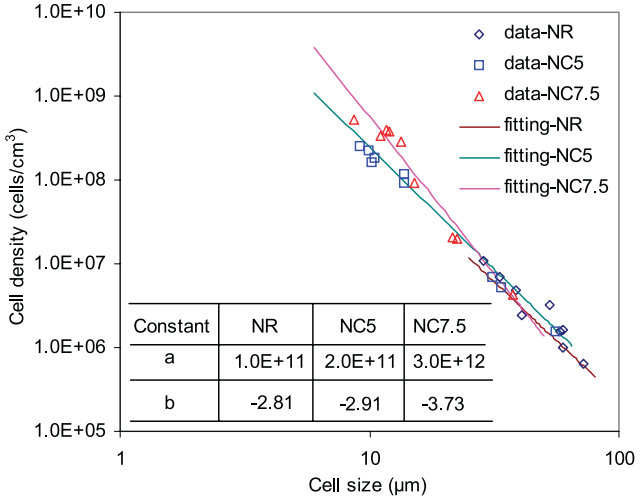

Constant	NR	NC5	NC7.5
a	1.0E+11	2.0E+11	3.0E+12
b	-2.81	-2.91	-3.73

Fig. 8. Log–log plot for the relationship between cell density and cell size in the microcellular injection molding process.

microcellular injection molding process for these tensile testing bars was the percentage of nanoclay in the PA6 matrix, it can be concluded that the nanoclay behaves as a microcell nucleation agent and promotes the smaller cell size and larger cell density which are desirable for attaining better mechanical properties. By careful scrutiny, it can also be seen that the cell wall surface of PA6 neat resin is much rougher than that of the nanocomposites. This indicates that the nanoclay addition generates a smoother cell wall surface as will be discussed later. It should also be noted that for all of the materials used, the cell size and cell density varied significantly with the microcellular injection molding conditions used, as reported elsewhere [38,42].

Through the examination of cell structure on the cross-sections both parallel and perpendicular to the flow direction, the general image of the cell distribution and orientation in microcellular parts can be obtained. Typically, as shown in Fig. 7, two different modes of cell distributions can be seen: The bell-shaped flow pattern parallel with the flow direction, and the cell size-reducing pattern normal to the flow direction. The bell-shaped flow pattern is due to the variation of shear stress, resembling the velocity profile and resulting in spherical cells near the center of the parts and elongated cells toward the solid boundary layer of the part. In the cell size-reducing pattern, the cell size seems to decrease towards the solid boundary layer of the part. It was suggested that the void volumes of the cells at the center and near the boundary layer are about the same [42].

3.2.2. Correlation between cell density and cell size

The cell size in the microcellular batch process can be made as small as a few microns. However, in a microcellular injection molding process of industrial scale, due to the limited SCF content and the complicated thermomechanical treatment, the cell size is larger. With the same polymeric material and SCF parameters, the cell

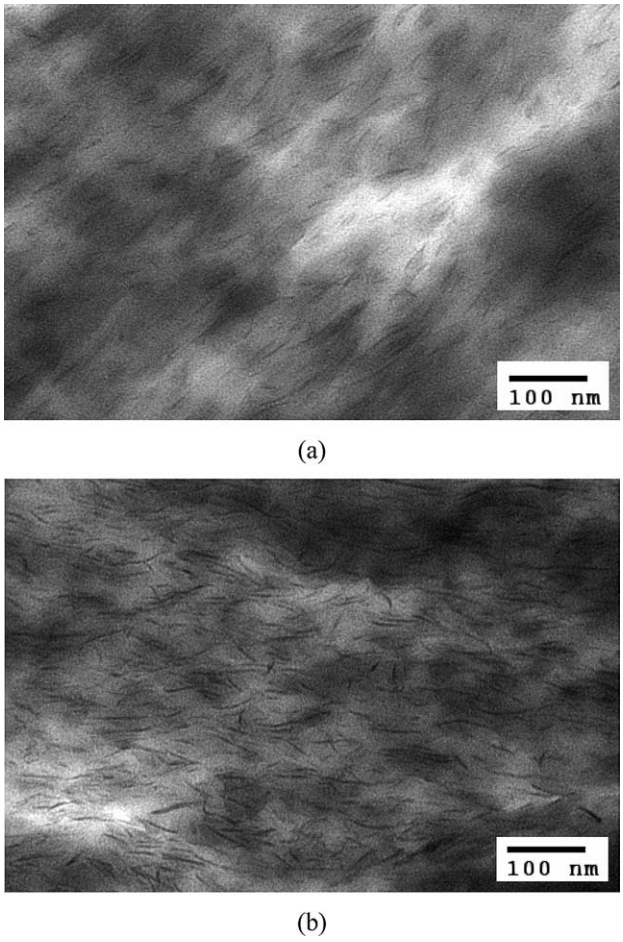

Fig. 9. TEM images of exfoliated PA6/MMT nanocomposites: (a) NC5, (b) NC7.5.

density and cell size follow the exponential rule under ideal conditions. In the microcellular injection molding process, the relationship between the cell density and the cell size is not so obvious. Besides the inherent material properties, many other effects are involved such as melt temperature, SCF content, injection shot size, injection speed, and injection unit and mold design. Interestingly, however, the correlation between the cell density and the cell size for all of the materials studied here seems to follow an exponential relationship as shown in Fig. 8, which can be expressed in the following form,

$$y = ax^b$$

where x and y represent the cell size and the cell density, respectively, and a and b are the inherent coefficients. b is a geometrical coefficient representing the three-dimensional cell distribution and normally has a value close to -3; a is an coefficient representing the compatibility and correlation of the material system with the processing system. For the materials NC5, NC7.5, and NR used in this study, x and y have the units of μm and cell/cm^3, respectively. The values for a and b are listed in the inset table of Fig. 8. The coefficient a has the unit of μm^{-3-b}. Depending on the material properties and the cell nucleation ability, the value of a varies from 1×10^{11} to 3×10^{12} for NR, NC5, and NC7.5.

3.2.3. TEM morphology

TEM results from JOEL JEM100CX TEM for the as-received raw pellets of NC5 and NC7.5 are shown in Fig. 9. Generally speaking, MMT particles are well dispersed in the polymer matrices, even though some small clay decks still exist. As expected, more clay platelets can be seen in the NC7.5 specimen than in the NC5 specimen.

For the solid PA6 nanocomposite dog-bone parts made via the injection molding process, the local preferential crystalline orientation of PA6 resin and nanoparticles across the thickness of the molded parts were investigated by Yalcin et al. using different structure characterization techniques including microbeam wide angle XRD, small angle X-ray scattering, and TEM [43]. It was found that nanoparticles induced high degrees of polymer orientation throughout the thickness of the molded parts. The high degree of molecular chain orientation observed in the nanocomposites was the result of the shear amplification effect that occurred in the small spaces between adjacent nanoplatelets of different velocity. The spatial distribution of nanoclays along the injection molding direction was discussed in another study [44]. Nanoclays in the layers near the four surfaces of the molded bar were parallel to their corresponding surfaces, whereas those in the bulk differed from the near-surface nanoclays and rotated themselves with respect to the injection molding direction [44].

Regarding the nanoplatelet alignment or orientation in microcellular injection molded parts, very little literature is available. Nam once reported that the clay platelets orient themselves in the polymer matrix along the cell wall direction [45], but the specimen studied was produced in a batch process with PP/MMT.

The TEM micrographs of nanoclay spatial dispersion for the NC5 specimen from the microcellular injection molding process are shown in Fig. 10. The nanoclay platelets near the cell wall are exfoliated and dispersed in the PA6 matrix. The nanoclay platelets orient along the surface curvature of the microcell wall as shown in Fig. 10. Between the microcell walls, the nanoclay platelets stretch out from the narrowed spatial isthmus. A more detailed study showed that some nanoclay tacktoids still exist, which indicates the difficulty of full exfoliation and dispersion of nanoclays. The nanoclay tacktoids were likely to be found in the microcellular junction area rather than in the region adjacent to the cell wall, as shown in Fig. 10.

3.2.4. Micromechanical pattern of nanoclay dispersion around the cells

As reported earlier, nanoplatelet orientation and distribution in the conventional injection molding process influences polymer crystallization [43]. In injection molded solid bars, the oriented nanoclay regions usually extend

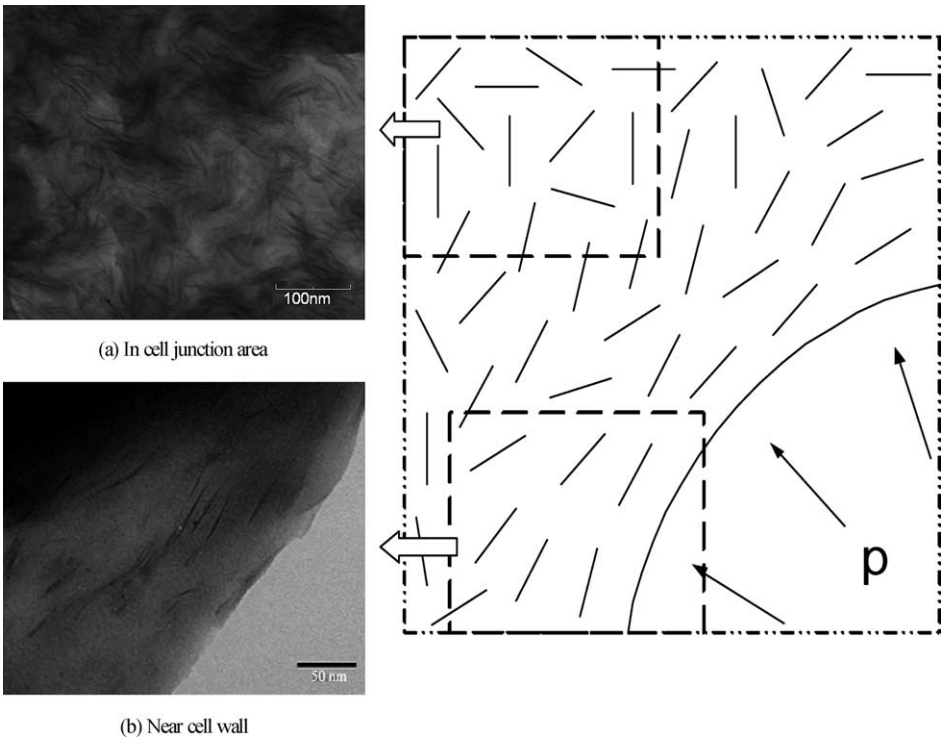

Fig. 10. TEM micrographs of nanoclay distribution and schematic orientation of nanoclay platelets in the cell junction area and near the cell wall.

1.2–2.0 mm beneath the surface of the bars. In this region, most MMT platelets align parallel to the surfaces of the part. So for standard tensile testing bars with a thickness between 3 and 4 mm, the entire cross section primarily has nanoclays orienting parallel to the surface and flow direction [43,46]. Due to spatial constraints from the cell walls in the microcellular injection molding process, immediately under the solid boundary layer, the orientation of nanoclays and that of the resulting crystalline structures differ from those in the solid injection molding process.

Between or among the cells, polymer and nanoclays flow or orient in the pseudo-convergent/divergent area. In the microcellular injection molding process, the cell nucleation starts at the injection nozzle. In the mold filling and cooling stages, including the course of the melt and gas solution flowing through the sprue and gate before entering the mold cavity, the cells continuously grow until the polymeric melt is vitrified or solidified so that the full constraint on the cell growth is exerted. With cell growth, the internal pressure of the microvoid will decrease so that the equilibrium state will be achieved by thermodynamics at the time the cell stops growing. During cell growth, the polymer around the cell is squeezed and stretched. The polymer chain and nanoclays are stretched along the cell wall curvature. In the junction area away from the cell walls, nanoclays orient randomly as shown in Fig. 10. The flow of polymeric melt and gas solution in the interspace of cells is governed both by the fluid dynamics and the cell growth dynamics. In this flow, the velocity field interacts dynamically with the internal cell pressure. To some extent, it is like a micro three-dimensional calendaring flow, but the fluid flow takes place while the geometry changes simultaneously.

3.2.5. *Effect of microcellular injection molding on nanoclay dispersion*

The XRD spectra of solid and microcellular injection molded nanocomposites with 5 and 7.5 wt% nanoclay are shown in Fig. 11(a) and (b), respectively. In the legends of Fig. 11, *f* and *t* indicate the XRD scanning direction along the flow direction and the transverse direction, respectively. Fig. 11(a) shows the different positions of nanoclay d_{001} peaks for the solid and microcellular nanocomposite parts. The peak at the smaller 2θ angle for the microcellular parts reflects the larger platelet spacing of the intercalated nanoclays. The larger spacing suggests the greater delaminating effect of microcellular injection molding process.

Fig. 11(b) shows that for higher nanoclay loading, the microcellular injection molding process also facilitates nanoclay intercalation and delamination. The clay spacing of the solid nanocomposite NC5 and NC7.5 parts is usually around 2.2 and 2.5 nm. Occasionally, some intercalated clay decks with a spacing of around 2.5 nm could also be detected in microcellular parts due to some uncertainty in the processing. But in general, the clay spacing of the microcellular parts became larger depending on the molding conditions. By adjusting microcellular molding conditions, a better result for delamination and exfoliation can be achieved. The peaks for microcellular nanocomposites also decrease in height and get broader as delamination increases. Based on the XRD results for the microcellular

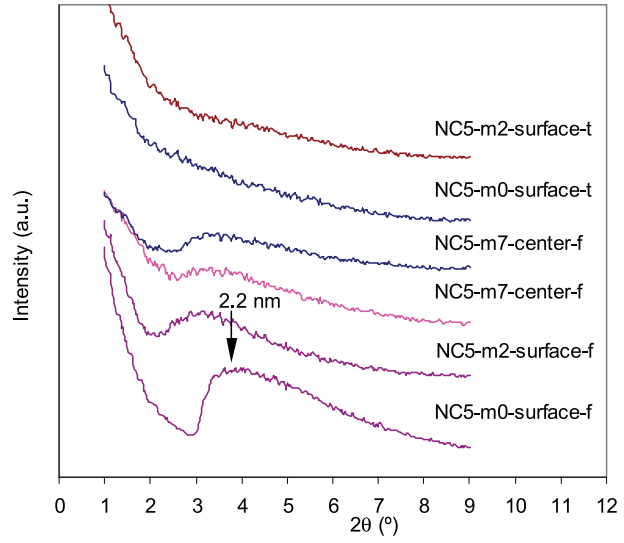

(a)

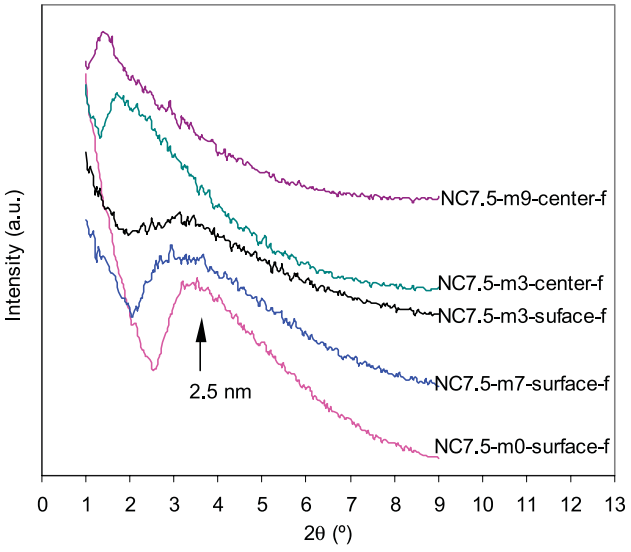

(b)

Fig. 11. XRD spectra of microcellular injection molded nanocomposites: (a) NC5, (b) NC7.5.

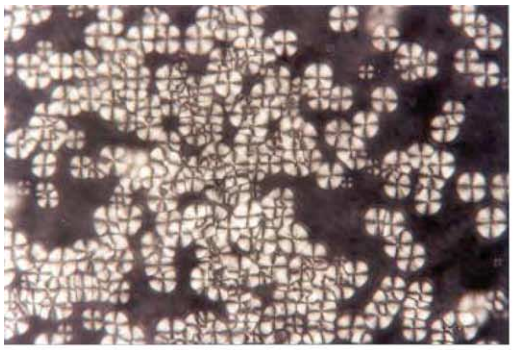

(a)

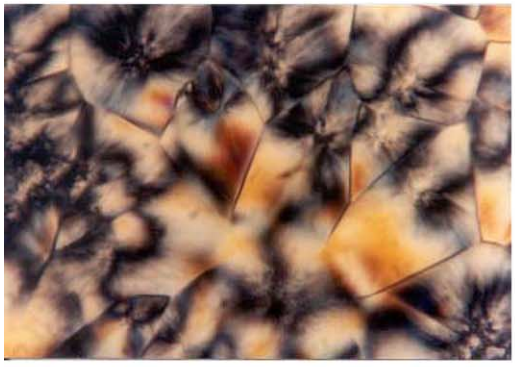

(b)

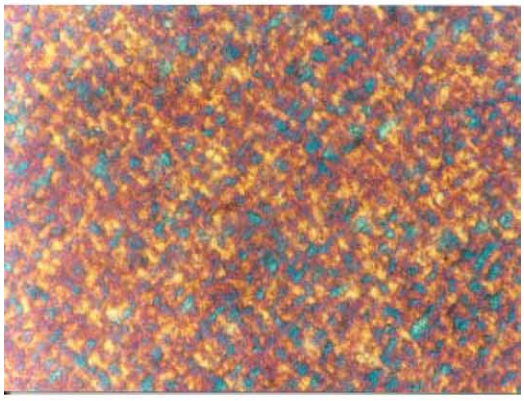

(c)

Fig. 12. Polarized optical micrographs of NC5 and NR: (a) NR spherulite at fast cooling, (b) impingement of NR spherulites at slow cooling, (c) NC5 at slow cooling.

molding trial 2 in Fig. 11(a), it can be seen that XRD patterns could differ with respect to the scanning direction. Additional XRD results from cross-sectioned surface layers suggest that the intercalated nanoclay on the surface may preferentially orient along the flow direction.

For the solid injection molding process, intercalation kinetics may be affected by the processing conditions, but the clay interlayer expansion depends mainly on the chemical compatibility of the polymer, the interlayer surfactant, and the clay surface [47–50]. Therefore, there may be an optimal degree of shear intensity where the best delamination and dispersion is reached [51]. However, with the assistance of SCF, even when favorable interactions between the polymer and the clay are not present, intercalated structures can still be produced. The increases in clay *d*-spacing for an SCF treated polymer can be consistently obtained regardless of the nature of the polymer, including purely hydrophobic polymers [52]. In the microcellular injection molding process, SCF penetrates easily into the gallery of intercalated nanoclays and diffuses readily into the polymer matrix. SCF also plasticizes polymers very efficiently and makes polymer molecules softer. As more smaller SCF molecules and more polymer

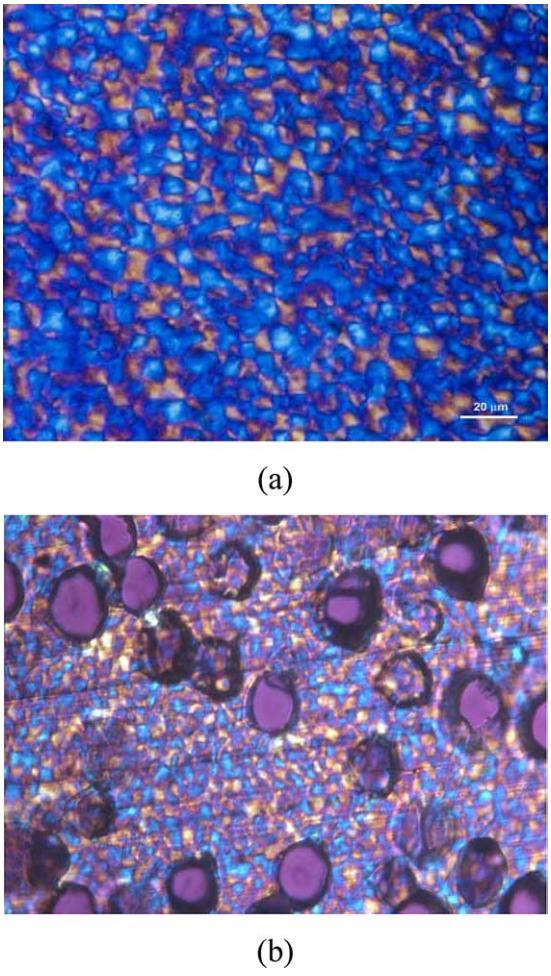

Fig. 13. Polarized optical micrographs of NR injection molding specimens: (a) The center of solid sample, (b) the center of microcellular sample at molding trial 2.

molecules enter the clay gallery, the platelets are pushed apart and loose their ordered crystalline structure, even becoming disordered. The proper amount of shear stress eventually tips off the disordered plates and facilitates the dispersion of platelets in the polymeric matrix to form the exfoliated nanoclay structure. Since SCF can effectively reduce the viscosity and the glass transition temperature of the polymeric melt as well as the interfacial tension, the shear stress experienced by nanoclay platelets will be generally lower than that in the solid injection molding process.

3.2.6. POM morphology

PA6 differs from most other crystalline polymers in that under the usual conditions of processing, the resulting structure is more likely to be spherulitic. Fig. 12 shows the spherulitic crystal structures of PA6 neat resin samples made on a hot-stage with different cooling rates. With the fast cooling process, the single crystalline spherulite and the bundle of spherulites can be seen clearly. At the slow cooling rate, the impingement of neighboring spherulites is

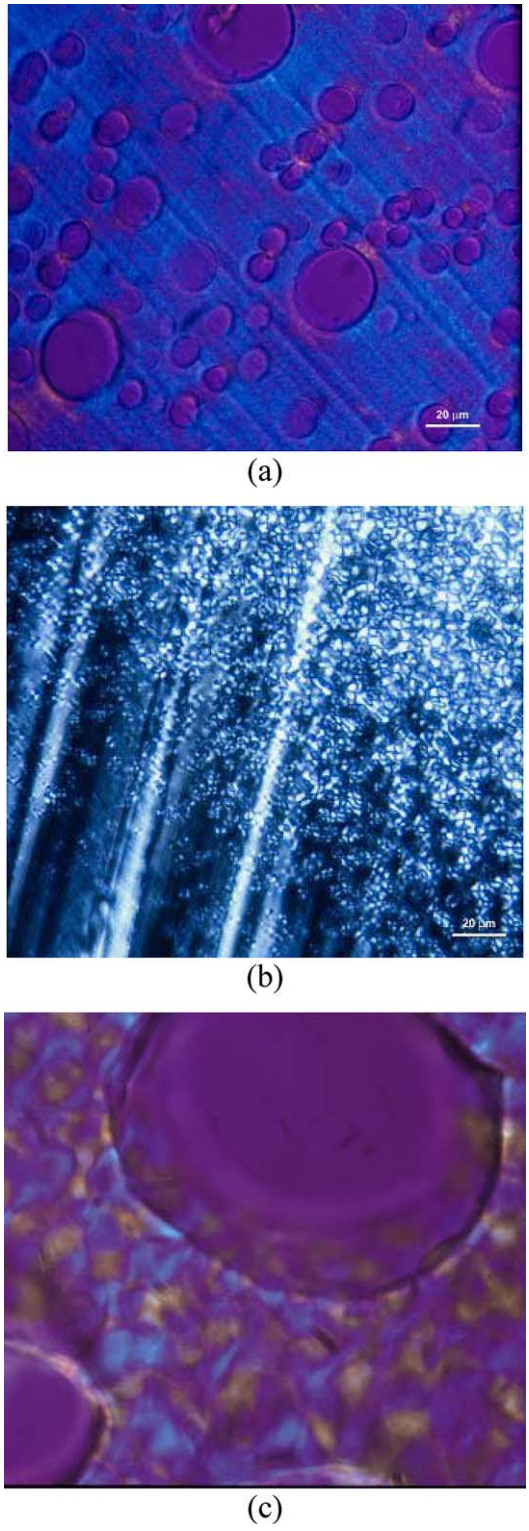

Fig. 14. Polarized optical micrographs of microcellular injection molded NR and NC5: (a) Center of NC5 at trial 3, (b) corner of NR at trial 2, (c) cell wall of NR at trial 2.

evident due to the spatial confinement around each crystalline spherulite. The sizes of the spherulites from the slow cooling process are larger due to the long duration of crystal growth. Fig. 12 also shows the POM graphs of the

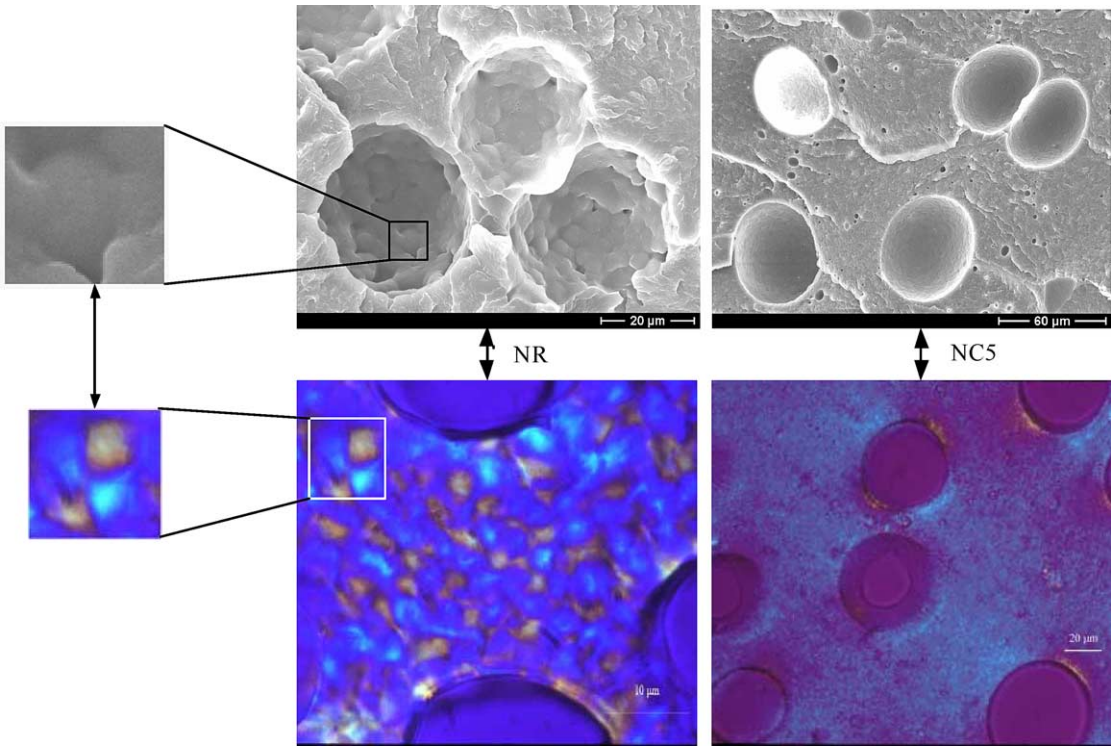

Fig. 15. Correlation between crystalline size and cell wall surface smoothness of microcellular NR and NC5 samples at molding trial 3.

crystalline structures of nanocomposite NC5 on a hot-stage. Under the fast cooling condition, the crystalline structure is nearly indiscernible. Nevertheless, a variety of non-spherulitic structures can be obtained with the slow cooling procedure for both NC5 and NC7.5. The crystalline structures of NC5 and NC7.5 are very similar. This suggests that the addition of nanoclay interrupts the development of complete spherulites, which may create anisotropic crystalline structures in nanocomposites [53].

The POM graphs for the specimens from the center of the injection molded NR bars are shown in Fig. 13. The solid specimen displays the larger crystalline structures and the structures obtained seem to be slightly impinged spherulites. The spherulites in the solid specimen are up to 20 μm in size. Compared to the crystalline structures from the hot-stage with the slow cooling process, the injection molded specimen has an obviously smaller crystalline structure. Compared with the injection molded solid NR counterpart, the molded microcellular NR part has a relatively smaller crystalline structure, but their crystalline structures are essentially similar. It seems possible that the larger number of crystallization sites are obtained during the microcellular injection molding process.

The crystalline structures of microcellular injection molded nanocomposite NC5 are shown in Fig. 14(a). The shapes and sizes of the crystalline structures could not be detected by POM at a magnification of 100 when the oil-immersion technique was used. The number of crystalline spot sites of both microcellular nanocomposites NC5 and NC7.5 are apparently much higher than that of the crystalline spherulites of microcellular neat resin NR, owing to the nucleation and confinement effect imposed by the addition of nanoclay. This suggests that the nanoclay is also an effective nucleating agent for PA6 crystalline structures.

Fig. 14(b) shows optical micrographs taken at the corner of the cross-sectioned microcellular NR sample. At the corner or along the boundary layer, small single crystalline spherulites can be clearly seen. The spherulite size increases gradually from the boundary layer to the center of the part. At the center, each crystalline spherulite likely impinges with the neighboring one due to the large difference in thermal histories between the boundary layer and the center of the part. Interestingly, although pure PA6 tends to form spherulitic structures, among all the nine microcellular injection molding trials and the solid injection molding experiment, only the specimens from those trials with the intermediate level (level 2) melt temperature setting clearly present those individual spherulitic structures. According to the DOE analysis, this melt temperature level yields the relatively better tensile properties of microcellular injection molded NR parts. In the area close to the skin, the solid boundary layer appears as a transparent beltline. This is due to the very fast cooling process and the formation of much smaller crystalline structures in this region. Occasionally, bundles of small crystalline spherulites can be found in the area near the surface; they are similar to those of some specimens from hot-stage compression.

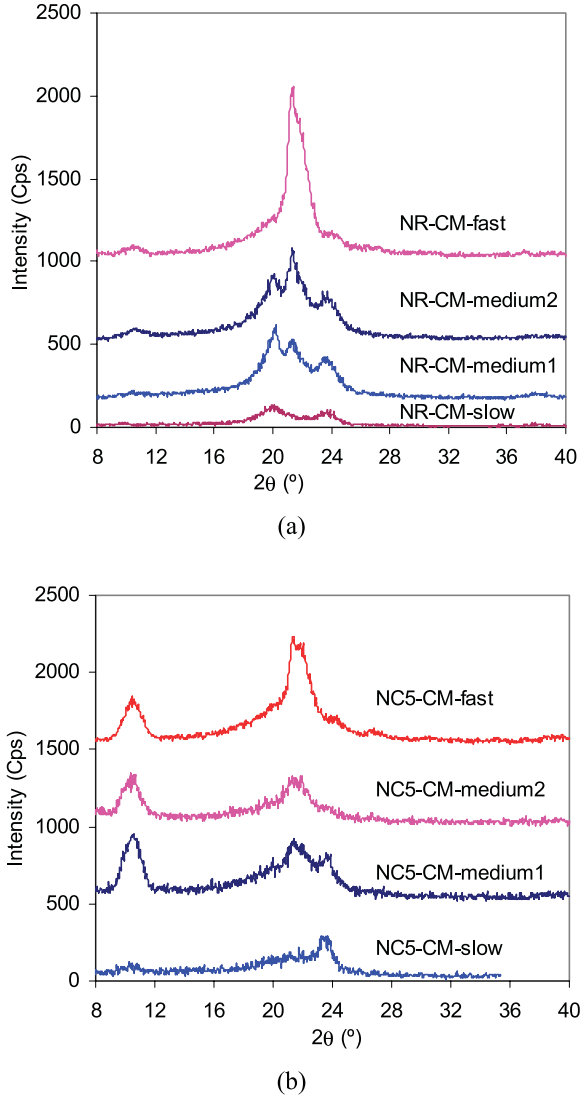

Fig. 16. XRD spectra for compression molded specimens at different cooling rates: (a) NR, (b) NC5.

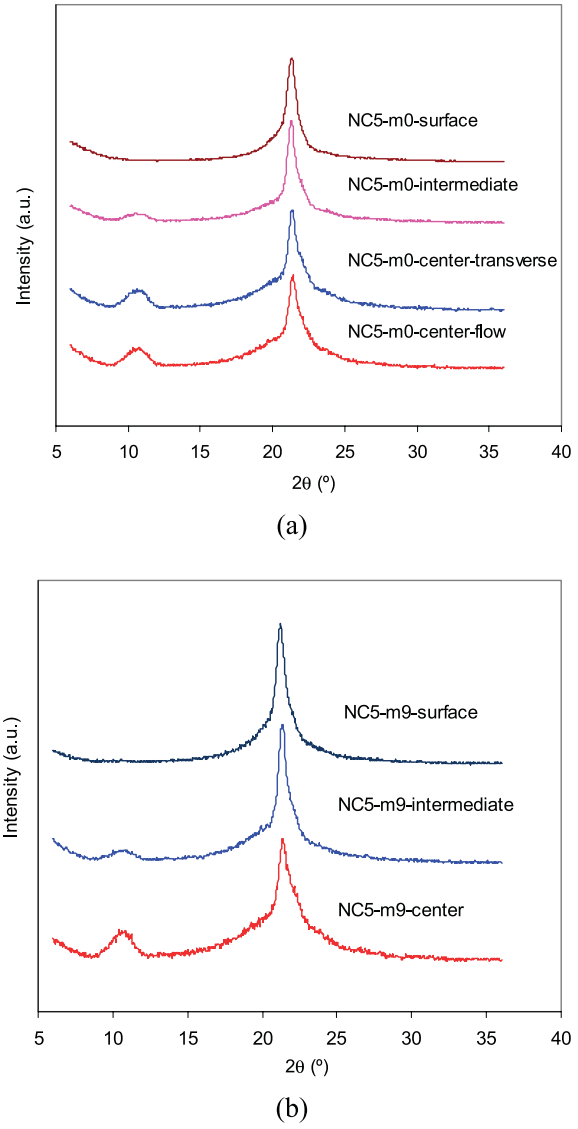

Fig. 17. XRD spectra for injection molded nanocomposite NC5 specimens at different planes from surface to center: (a) Solid, (b) microcellular.

3.2.7. Crystal size with respect to cell wall surface

In order to distinguish the crystalline structures of the cell walls and their surrounding solid materials, slightly thicker POM microcellular NR and microcellular nanocomposite NC5 specimens were used to demonstrate the detailed cell wall structures, as exemplified in Fig. 14(c). For all of the materials used, the crystalline structures on the wall surface displayed the same pattern as on their surrounding areas, and no boundary layer on the cell wall could be seen.

Microcellular nanocomposites have smaller cell structures, smoother cell wall surfaces, and better tensile properties than microcellular neat resin. The cell wall quality may have a direct impact on the toughness, impact, and tensile properties of the part. The comparison of the crystalline structure of the microcellular part and the cell wall smoothness is shown in Fig. 15. For the microcellular neat resin NR part from molding trial 3, the diameter of crystalline spherulites is about 6–8 μm. Coincidently, the characteristic roughness of the cell wall has about the same dimension. Therefore, it can be claimed that that the cell wall smoothness is determined by the size of the crystalline structure and, therefore, is dependent on the crystallization behavior of the material. The same conclusion for microcellular nanocomposites can be drawn by comparing the cell wall structure with the crystalline structures of microcellular nanocomposite NC5 in Fig. 15. The crystallization and thermal behavior of microcellular injection molded nanocomposites is discussed in Ref. [54].

3.2.8. XRD results for crystal structures

Fig. 16(a) shows the XRD spectra for compression molded NR specimens with different cooling rates. All samples from the compression molded process contain either some or all of peaks at $2\theta \approx 20$ and 23.7°, corresponding to the α_1 and α_2 peaks of the α-form, and

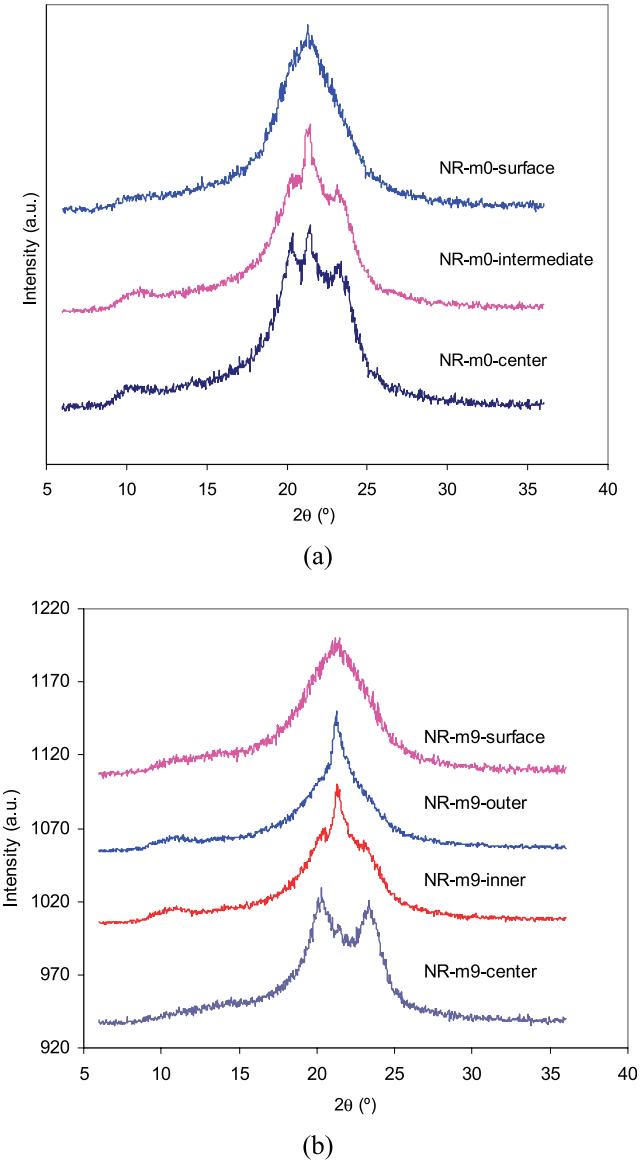

Fig. 18. XRD spectra for injection molded neat resin NR specimens at different planes from surface to center: (a) Solid, (b) microcellular.

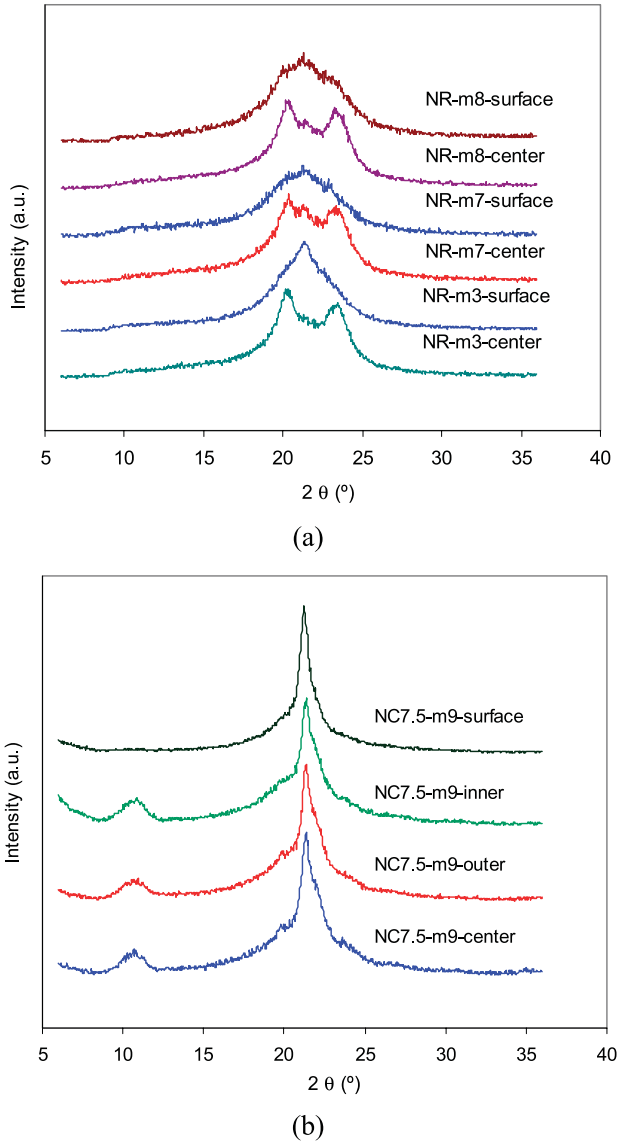

Fig. 19. XRD spectra for microcellular injection molded samples: (a) Neat resin NR with different molding conditions, (b) nanocomposite NC7.5 at different planes from surface to center.

21.3° indicative of the γ-form. Under the fast cooling condition, the predominant γ peak and the shoulders of α peak are seen. With the slow cooling rate, two predominant α peaks appear and the γ peak at 21.3° disappears. As the cooling rate decreases, the crystallization temperature increases, the amount of γ-form gradually decreases, and the amount of α-form gradually increases. Although no apparent microscopic structures can be seen to distinguish α-form and γ-form crystalline structures for PA6, it is recognized that the α-form is favored to grow more readily due to its higher thermal stability than the γ-form when the cooling rate decreases and the temperature is kept high. Rapid cooling forces crystallization to occur at low temperatures where the rate is limited by polymer chain mobility; mobility limitations may be the cause for favoring the γ-form. Slow cooling, on the other hand, allows crystallization to occur at higher temperatures where the rate is mainly dominated by the driving force or degree of undercooling.

For the compression molded nanocomposite NC5, at the fast and medium cooling rates, the γ-form of 21.3° is predominate. At the very slow cooling rate, only a sharp α crystalline peak at around 23.7° and a trace of γ crystalline peak around 21.3° are present as shown in Fig. 16(b). This similar phenomena was reported earlier with a hot-stage [55]. Even with the nanoclay contents increased from 5 to 7.5 wt%, under the very slow cooling condition, the strong γ crystalline signal at 21.3° shows up, but another sharp α crystalline peak at 23.7° can still be seen. By adding more nanoclay, the intensity of the γ-form is increased. This suggests that the exfoliated nanoclay promotes the nucleation and formation of γ crystals.

Clearly, both the addition of nanoclay and the cooling rate play important roles in the polymorphic behavior of the PA6 nanocomposite.

One major effect of MMT nanoclay in the PA6 matrix is to increase the initial crystallization rate of PA6. The high intensity of single α crystalline peak at 23.7° for nanocomposites at the slow cooling condition is probably due to the structural feature of the hexagonal lattice in which the surface of the (110) layer of MMT could prefer the crystal arrangement along the (110) plane of PA6 during crystal formation.

The typical XRD results for microcellular injection molded NR, NC5, and NC7.5 specimens from the same molding conditions are shown in Figs. 17–19. For both NC5 and NC7.5 nanocomposites, the predominant γ-form peak with shoulders on both sides representing the traces of α-form crystals can be seen clearly, as exemplified in Fig. 17. These γ-form peaks exhibit single crystalline reflection which is the merged results from the γ-form triplet (200), (001), and (201). This form of PA6 has the monoclinic structure with $a=9.33$ Å, $b=16.88$ Å, $c=4.78$ Å, and $\beta=121°$ [6,56]. With this γ-form structure only, the peak is sharp and symmetric at about 21.3°. Based on all of the experimental results in this study, even with the high nanoclay loading and on the molded bar surface, the only γ-form crystal formation is unlikely to happen, which is contradicted with some reports in the literature [33]. However, for the microcellular neat resin NR, as shown in Fig. 18, the central plane shows two distinct peaks at about 20 and 23.7° for the α-form crystalline structures. The left peak (α_1) presents as an α(200) plane, while the right peak (α_2) appears as the result of an α-form doublet (002) and (202) of the diffraction spots. The currently accepted α-form structure is of the monoclinic characteristics of $a=9.56$ Å, $b=17.24$ Å, $c=8.01$ Å, and $\beta=67.5°$ [57]. As for the microcellular neat resin, the central plane of the part shows two distinct peaks for (α_1) and (α_2), respectively. The surface of the part has a single broad peak merged from (α_1) at 20°, (α_2) at 23.7°, and the γ-form at 21.3° on the base of the amorphous fraction.

Regarding the peak at about 10.8°, the reports in the literature are still not consistent [33]. In this study, when the neat resin NR was used in both solid and microcellular injection molding, only a trace of the peak at about 10.8° could be seen at the area between the center and the skin or under certain molding conditions. For the nanocomposites NC5 and NC7.5, this peak could not be detected on the surface or in the skin layer, but this broad distinct peak was present in the central region of the parts. This peak used to be assigned as γ(020) and represents the anisotropic orientation of PA6 γ crystalline structures [35,43,58,59]. The explanation lies in that the nanoclay alters the structural orientation of γ-form texture. This γ-form is favored to grow at certain cooling rates. On the part surface, the γ-form structure is smaller, and this anisotropic effect is not significant.

Fig. 17(a) shows the XRD data on the planes with different distances to the surface of the solid nanocomposite NC5 part. The slightly different breadths of the peaks show that there is a slight variation on the relative fractions of both the α-form and γ-form crystalline structures from the center to the surface of the microcellular part. Compared with the XRD results for microcellular nanocomposites in Fig. 17(b), no significant changes regarding the crystalline structures are observed. This implies that the microcellular injection molding process does not change the crystallization mechanism or crystalline structures of the PA6 nanocomposite greatly. The XRD results on the intermediate plane along the flow direction and the transverse direction indicate no significant differences in the crystalline structures in different directions.

There may be a weak preferential orientation of crystalline structures in the core of microcellular parts. The reasons lie in the diminutive size of crystalline structures and the microcell formation in the molding process. As discussed above, nanoclays have a special alignment in the junction area of cells. Therefore, the local orientation of PA6 crystalline structures along MMT nanoclays in microcellular parts is less ordered as are MMT nanoclays in molded solid parts.

Microcellular injection molded parts in this study usually had a solid boundary layer about 300–400 μm thick depending on the material type used and the molding conditions. This size is comparable to the thickness of the layer where the MMT nanoclays are reportedly well oriented in the solid part [44]. For the injection molded solid and microcellular neat resin parts, the XRD results from the different planes in the parts are compared in Figs. 18 and 19. As shown in Fig. 18(a), due to the rapid cooling and solidifying process near the surface of the solid part, the strong γ-form signal can be easily seen. Down over the skin layer, the intensity of the γ-form crystalline dramatically decreases. Towards the part center, more α and less γ crystalline structures are seen due to the lower cooling rate and longer thermal history.

As shown in Fig. 18(b), the crystalline structure on the surface and the skin regions of the microcellular NR parts is similar to that of the solid parts. At the interface between the solid boundary layer and the microcellular core, a distinctively narrower peak at around 21.3° for the γ-form appears with the shoulders of the α-form. In the core of microcellular neat resin samples, the apparent γ-form peak disappears. Under most molding conditions, a lesser amount of the γ-form in microcellular NR parts was observed as compared to solid parts. This implies that the microcellular process changes the crystallization behavior of PA6 in the center of parts slightly. SCF perhaps decreases the supercooling temperature and also slightly reduces the cooling rate due to the low temperature and thermal conductivity of its small molecules. The crystalline structures in the core of the microcellular NR part correspond to the structure of the compression molded sample under the slow cooling

Table 4
Crystallinity data obtained from curve fitting microcellular neat resin NR XRD patterns

Molding trial no.	% MMT	Core				Skin			
		% α	% γ	Total (%)	% γ of total	% α	% γ	Total (%)	% γ of total
0	0.0	27.9	3.6	31.5	11.3	15.9	8.7	24.6	35.4
1	0.0	25.0	1.5	26.5	5.8	18.5	9.6	28.1	34.3
2	0.0	17.7	5.1	22.8	22.4	16.6	10.8	27.4	39.5
3	0.0	18.0	2.7	20.7	12.9	15.3	6.9	22.2	31.3
4	0.0	22.2	1.5	23.7	6.4	19.7	7.3	27.0	26.9
5	0.0	22.9	3.1	26.0	11.8	20.8	11.0	31.8	34.5
6	0.0	21.8	5.8	27.6	20.9	18.5	12.6	31.1	40.5
7	0.0	19.3	4.9	24.2	20.1	17.5	7.8	25.3	31.0
8	0.0	19.0	3.3	22.3	14.9	14.1	9.9	24.0	41.1
9	0.0	26.1	5.5	31.6	17.3	21.6	11.7	33.3	35.0
Average	0.0	22.0	3.7	25.7	14.4	17.8	9.6	27.5	35.0

condition. This is due to a lower melting temperature of PA6 when the SCF is added. From the center to the surface, the increasing amount of γ and the decreasing amount of α were also observed as shown in Fig. 18(b). With the different microcellular molding conditions, the portions of α-form and γ-form crystalline structures vary both in the skin layer and the central region, as shown in Fig. 19(a). A detailed discussion on the crystallinity of microcellular parts is presented in a different paper [54].

Even though SCF may have an insignificant effect on the crystalline structure and part crystallinity, the addition of nanoclay to the microcellular injection molding process does have an influence on the crystalline structure and crystallinity. For the solid and microcellular nanocomposite NC7.5 samples, as in the case of NC5, when more nanoclay is dispersed in the PA6 matrix, their skin regions are still γ-form dominant; in their core regions, the γ-form is also promoted, as shown in Fig. 19(b). By comparing this with the results of injection molded and compression molded neat resin samples, the conclusion can be drawn that the MMT nanoclay addition facilitates the α-form transformation into the γ-form and alters the relative proportions of the α-form and the γ-form crystalline structures in the skin and core regions.

Even though there may be some limitations of using X-ray and DSC methods to evaluate the relative crystallinity or the crystallization index, the XRD deconvolution method still renders a way to quantitatively estimate the crystalline structural content. For microcellular injection molded parts, crystallization indices are listed in Tables 4–6. The data in these tables indicate that the skin layer has a higher relative crystallinity than the core of the microcellular part. The addition of nanoclay reduced the crystallinity but promoted γ-form formation. In the microcellular injection molded part, a single form of crystalline structure could not be found. The lower crystallinity of microcellular nanocomposites is due to the presence of dispersed nanoclay platelets and the addition of SCF. The presence of dispersed nanoclay and SCF confines the movement of polymer molecular chains to be incorporated into growing crystalline lamella and prevents large crystalline domains from forming due to the large nanoclay barrier and the low degree of supercooling.

4. Conclusions

The microstructures and mechanical properties of

Table 5
Crystallinity data obtained from curve fitting microcellular nanocomposite NC5 XRD patterns

Molding trial no.	% MMT	Core				Skin			
		% α	% γ	Total (%)	% γ of total	% α	% γ	Total (%)	% γ of total
0	5.0	15.0	8.1	23.1	34.9	8.3	16.9	25.2	67.2
1	5.0	18.9	4.9	23.8	20.7	14.6	10.6	25.2	42.0
2	5.0	10.5	4.3	14.8	29.1	9.4	12.3	21.7	56.6
3	5.0	16.6	7.3	23.9	30.6	9.8	16.6	26.4	63.0
4	5.0	10.9	8.0	18.9	42.4	9.8	13.1	22.9	57.2
5	5.0	9.3	5.3	14.6	36.0	9.8	14.9	24.7	60.5
6	5.0	21.5	8.6	30.1	28.6	18.0	13.8	31.8	43.4
7	5.0	13.8	5.7	19.5	29.4	11.9	10.9	22.8	48.0
8	5.0	13.8	6.2	20.0	30.9	13.4	11.6	25.0	46.3
9	5.0	17.8	4.9	22.7	21.7	11.6	16.5	28.1	58.7
Average	5.0	14.8	6.3	21.1	30.4	11.7	13.7	25.4	54.3

Table 6
Crystallinity data obtained from curve fitting microcellular nanocomposite NC7.5 XRD patterns

Molding trial no.	% MMT	Core				Skin			
		% α	% γ	Total (%)	% γ of total	% α	% γ	Total (%)	% γ of total
0	7.5	15.2	6.2	21.4	28.8	12.0	12.3	24.3	50.7
1	7.5	12.8	5.3	18.1	29.3	10.6	9.5	20.1	47.4
2	7.5	15.6	5.1	20.7	24.7	12.9	9.4	22.3	42.0
3	7.5	15.4	4.7	20.1	23.4	10.1	12.1	22.2	54.6
4	7.5	11.6	6.2	17.8	35.0	7.7	13.3	21.0	63.2
5	7.5	15.2	3.8	19.0	20.2	10.8	9.7	20.5	47.3
6	7.5	16.8	5.1	21.9	23.3	12.5	9.5	22.0	43.4
7	7.5	17.1	5.8	22.9	25.3	15.3	14.3	29.6	48.2
8	7.5	12.3	4.1	16.4	25.0	10.1	10.1	20.1	50.0
9	7.5	16.3	6.5	22.8	28.3	11.6	14.0	25.6	54.6
Average	7.5	14.8	5.3	20.1	26.3	11.4	11.4	22.8	50.1

microcellular injection molded nanocomposites were investigated. With the addition of nanoclay in microcellular injection molded parts, the growth of α-form crystals was suppressed and the formation of γ-form crystals was promoted. Nanoclay is an effective nucleation agent not only for microcells but also for PA6 crystals. The cell wall smoothness was dictated by the size of crystalline structures. With the addition of nanoclay, a small and dense microcellular structure with a smooth cell wall surface was achieved. Appropriate amounts of nanoclay and optimal molding conditions produced finer and denser microcell structures and lead to better mechanical properties. With the synergetic effect of supercritical fluid and nanoclay, the normalized toughness was improved for the PA6 part. Due to the micromechanical effect of PA6 and nanoclay in the junction area of the cells, the nanoclay and crystalline structures were weakly oriented in the core of the molded parts. Supercritical fluid in the microcellular process facilitated nanoclay intercalation and exfoliation as well as dispersion in the PA6 matrix. Nanoclays had a greater effect on PA6 crystalline structures while the dissolved gas only slightly influenced the crystalline transformation.

Acknowledgements

The authors would like to thank Dr Daniel F. Caulfield, Dr Shaoqin Gong, Dr Rebecca Ibach, and Dr Craig M. Clemons for their helpful discussions and experimental assistance. The authors would also like to acknowledge the RTP Company, USA, for generously donating the experimental materials used in this study and the Kaysun Corporation, USA, for assisting with the microcellular injection molding experiments. Great assistance is acknowledged from the Forest Products Laboratory (FPL), USDA, Materials Research Science and Engineering Center (MRSEC), and Biological and Biomaterials Preparation, Imaging, and Characterization (BBPIC) Laboratory at the University of Wisconsin-Madison. Part of this research is supported by the National Science Foundation (DMI 0323509) and the I&EDR award from the University of Wisconsin-Madison.

References

[1] Usuki A, Kojima Y, Wkawsumi M, Okada A, Fukushima Y, Kurauchi T, et al. J Mater Res 1993;8(5):1179.
[2] Vaia RA, Giannelis EP. Macromolecules 1997;30(25):8000.
[3] Alexandre M, Dubois P. Mater Sci Eng Rep 2000;28:1.
[4] Gogolewski S, Pennings AJ. Polymer 1997;18:654.
[5] Illers KH, Haberkorn H, Simák P. Makromol Chem 1972;158:285.
[6] Xenopoulos A, Clark ES. In: Kohan MI, editor. Nylon plastics handbook. New York: Hanser; 1995.
[7] Bureau MN, Denault J, Cole KC, Enright GD. Polym Eng Sci 2002; 42(9):1897–906.
[8] Penel-Pierron L, Depecker C, Séguéla R, Lefebvre JM. J Polym Sci, Part B 2001;39:484.
[9] Khanna YP, Kuhn WP. J Polym Sci, Part B 1997;5:2219.
[10] Illers KH. Makromol Chem 1978;179(2):497–507.
[11] Kumar V, Wells JE. SPE ANTEC Tech Pap 1992;38:1508.
[12] Martini JE, Waldman FA, Suh NP. SPE ANTEC Tech Pap 1982;28: 674.
[13] Baldwin DF, Suh NP. SPE ANTEC Tech Pap 1992;38:1503.
[14] Seeler KA, Kumar V. J Reinf Plast Compos 1993;12:359.
[15] Cha SW, Suh NP. SPE ANTEC Tech Pap 1992;37:1527.
[16] Kumar V, Suh NP. Polym Eng Sci 1990;30:1323.
[17] Park CB, Suh NP. ASME Cell Polym 1992;38:69.
[18] Geol SK, Beckman EJ. Polym Eng Sci 1994;34(14):113.
[19] Baldwin DF, Suh NP, Shimbo M. ASME Cell Polym 1992;38:109.
[20] Park CB, Suh NP. SPE ANTEC Tech Pap 1993;39:1818.
[21] Baldwin DF, Suh NP, Shimbo M. ASME Cell Polym 1992;38:109.
[22] Baldwin DF, Park CB, Suh NP. Polym Eng Sci 1996;36(10):1425.
[23] Shimbo M, Nishida K, Heraku T, Iijima K, Sekino T, Terayama T. Foams 1999, First International Conference on Thermoplastic Foam, Parsippany, New Jersey 1999. p. 132.
[24] Shimbo M, Kawashima H, Yoshitani S. Foams 2000, Second International Conference on Thermoplastic Foam, Parsippany, New Jersey 2000. p. 162.
[25] Jacobsen K, Pierick D. SPE ANTEC Tech Pap 2000;58(2):1929.
[26] Xu J, Pierick D. J Injection Molding Tech 2001;5(3):152.
[27] Kumar V, Weller JE. ACS Symp Ser 1997;669:101.
[28] Park CB. In: Lee S, editor. Foam extrusion. Philadelphia: Technomic Publishing Co. 2000.
[29] Cooper AI. J Mater Chem 2000;10(2):207.

[30] Michaeli W, Pfannschmidt O, Habibi-Naini S. Kunststoffe 2002; 92(6):48.
[31] Wang H, Zeng C, Elkovitch M, Lee LJ, Koelling KW. Polym Eng Sci 2001;41(11):2036.
[32] Svoboda P, Zeng C, Wang H, Yang Y, Li H, Lee LJ, et al. 2002 NSF DMII Grantee and Research Conference, San Juan, Puerto Rico 2002.
[33] Fornes TD, Paul DR. Polymer 2003;44:3945–61.
[34] Ho J, Wei K. Macromolecules 2000;33:5181.
[35] Zheng J, Siegel RW, Toney CG. J Polym Sci, Part B 2003;41: 1033–50.
[36] van Melick HGH, Govaert LE, Meijer HEH. Polymer 2003;44: 2493–502.
[37] Uribe-Arocha P, Mehler C, Puskas JE, Altstädt V. Polymer 2003;44: 2441–6.
[38] Yuan M, Turng L, Gong S, Caulfield D, Hunt C, Spindler R. Polym Eng Sci 2004;44(4):673–86.
[39] Mohd Ishak ZA, Berry JP. J Appl Polym Sci 1994;51:2145.
[40] Chow WS, Mohd Ishak ZA, Karger-Kocsis J, Apostolov AA, Ishiaku US. Polymer 2004;44:7427–40.
[41] Penel-Pierron L, Séguéla R, Lefebvre JM, Miri V, Depecker C, Jutigny M, et al. J Polym Sci, Part B 2001;39:1224.
[42] Yuan M, Winardi A, Gong S, Turng L. Polym Eng Sci 2005;45(6): 773–88.
[43] Yalcin B, Valladares D, Cakmak M. Polymer 2004;44:6913–25.
[44] Yu Z, Yang M, Zhang Q, Zhao C, Mai Y. J Polym Sci, Part B 2003; 41(11):1234–43.
[45] Nam PH, Maiti P, Okamoto M, Kotaka T, Nakayama T, Takda M, et al. Polym Eng Sci 2002;42(9):1907–18.
[46] Varlot K, Reynaud E, Kloppfer MH, Vigier G, Varlet J. J Polym Sci, Part B 2001;39:1360–70.
[47] Vaia RA, Jandt KD, Kramer EJ, Giannelis EP. Macromolecules 1995; 28:8080.
[48] Vaia RA, Giannelis EP. Macromolecules 1997;30:8000.
[49] Balazs AC, Singh C, Zhulina E. Macromolecules 1998;31:8370.
[50] Ginzburg VV, Balazs AC. Macromolecules 1999;32:5681.
[51] Dennis HR, Hunter DL, Chang D, Kim S, White JL, Cho JW, et al. Polymer 2001;42:9513–22.
[52] Garcia-Leiner M, Lesser AJ. Polym Prepr 2004;45(1):520–1.
[53] Yalcin B, Cakmak M. Polymer 2004;45:2691–710.
[54] Yuan M, Turng L, Caulfield DF, Polym Eng Sci, in review.
[55] Wu T, Chen E, Liao C. Polym Eng Sci 2002;42(6):1141–50.
[56] Holmes DR, Bunn CW, Smith DJ. J Polym Sci 1955;17:159.
[57] Arimoto H. J Polym Sci, Part A 1964;2:2283.
[58] Varlot K, Reynaud E, Kloppfer MH, Vigier G, Varlet J. J Polym Sci, Part B 2001;39:1360–70.
[59] Kojima Y, Usuki A, Kawasumi M, Okada A, Kurauchi T, Kamigaito O, et al. J Polym Sci, Part B 1994;32:625–30.